SUPPORTING INFORMATION FOR

Machine Learning Assisted Screening of Cyano-Enriched Additives to Mitigate Elevated Temperature Degradation of $LiPF_6$-Carbonate Electrolyte

Xiangchun Zhuang[abc+], Lixin Qiao[ac+], Fanteng Meng[abc], Xiaofan Du[ac], Lixuan Yang[abc], Shenghang Zhang[ac], Bin Xie[ac], Cizhen Luo[d], Jinran Sun[ac], Lang Huang[ac], Shitao Wang[ac], Zili Cui[ac]*, Shanmu Dong[abc], Gaojie Xu[abc]*, Guanglei Cui[abc]*

[a] X. Zhuang, Dr. L. Qiao, F. Meng, Dr. X. Du, L. Yang, Dr. S. Zhang, B. Xie, Dr. J. Sun, Prof. L. Huang, Dr. S. Wang, Prof. Z. Cui, Prof. S. Dong, Prof. G. Xu, and Prof. G. Cui

Qingdao Institute of Bioenergy and Bioprocess Technology, Chinese Academy of Sciences

Qingdao New Energy Shandong Laboratory,

Qingdao 266101, China

E-mail: cuigl@qibebt.ac.cn, xugj@qibebt.ac.cn, cuizl@qibebt.ac.cn

[b] X. Zhuang, F. Meng, L. Yang, Prof. S. Dong, Prof. G. Xu and Prof. G. Cui

Center of Materials Science and Optoelectronics Engineering

University of Chinese Academy of Sciences

Beijing 100049, China

[c] X. Zhuang, Dr. L. Qiao, F. Meng, Dr. X. Du, L. Yang, Dr. S. Zhang, B. Xie, Dr. J. Sun, Prof. L. Huang, Dr. S. Wang, Prof. Z. Cui, Prof. S. Dong, Prof. G. Xu, and Prof. G. Cui

Shandong Energy Institute

Qingdao 266101, China

[d] C. Luo

Yibin Fengyuan New Material Co., Ltd

Yibin 644000, China

[+] These authors contributed equally to this work.

This PDF file includes:
Figures S1 to S35

Methods

Synthesis of lithium bis(1,2-dihydroxyethane-1,1,2,2-tetracarbonitrile)borate (LiBTCB)

Trimethylsilyl cyanide (TMSCN, 50 g) was placed in a 200 mL round-bottom flask, followed by the slow addition of oxalyl chloride (Aladdin, 16 g) to the TMSCN solution in an ice bath. The mixture was stirred for 1 h at 0 °C. Subsequently, the ice bath was removed, and the reaction was allowed to proceed at room temperature for 5 days, resulting in the intermediate compound 2,2,7,7-tetramethyl-3,6-dioxa-2,7-disilaoctane-4,4,5,5-tetracarbonitrile (TDSTCN). Purification of TDSTCN was achieved through recrystallization in 1,2-dimethoxyethane (DME, Aladdin, 15 mL) performed twice, yielding approximately 41%. ^{1}H NMR (400 MHz, $CDCl_3$): δ 0.25 (s, 18H). $^{13}C\{^{1}H\}$ NMR (101 MHz, $CDCl_3$): δ 110.8 (s, CN), 70.0 (s, C-O), 0 (s, $Si(CH_3)_3$). $^{29}Si\{^{1}H\}$ NMR (79.5 MHz, $CDCl_3$): δ 36.6 (s). Subsequently, TDSTCN (2 mmol) was dissolved in propylene carbonate (PC, Aladdin, 2 mL), then lithium tetrafluoroborate ($LiBF_4$, Aladdin, 2.4 mmol) was added and the reaction was maintained at 60 °C for 10 h to obtain LiBTCB (yield >90%). Finally, 1 mmol LiBTCB solid powder was resolved in 1 ml DME and precipitated to obtain the target product.

Preparation of electrodes, electrolytes, cells and electrochemical measurements

The baseline electrolyte, consisting of 1 M $LiPF_6$ dissolved in a mixture of ethylene carbonate and ethyl methyl carbonate (EC/EMC, 3:7 v/v), referred to as BE, was purchased from DoDoChem (China). To prepare modified electrolytes, 10 wt.% fluoroethylene carbonate (FEC) was added to BE to produce BE + FEC. Subsequently, BE + FEC was further modified by the addition of 0.5 wt.% lithium bis(1,2-dihydroxyethane-1,1,2,2-tetracarbonitrile)borate (LiBTCB). All materials were stored and prepared in a glove box filled with argon gas (O_2 and H_2O contents below 0.1 ppm).

High-capacity NCM811 cathode (12 mm, 17.2 mg cm^{-2}) and SiO_x-Gr anode (14 mm) were purchased from Tafel New Energy Technology Co., Ltd. (China). 2032 coin-type NCM811/SiO_x-Gr full cells (N/P ratio ~ 1.1) were assembled using PP separator

(Celgard 2500) and the prepared electrolytes above (80 μL) in an Ar-filled glove box. The electrochemical tests of these cells were implemented using a NEWARE system (2.7-4.25 V, CT-4008T-5 V 10 mA, NEWARE Technology Limited (China)) at 30 ℃ or 50 °C. And the full cells were charge/discharge at 0.2 C (1 C = 200 mA g^{-1}) in the first two pre-cycles, then held long-cycle rate at 0.5 C. For the self-discharge tests, the cells underwent two pre-cycles before being fully charged and held at 50 °C to monitor the voltage change. The SiO_x-Gr/Li half cells were assembled using 600 μm thick Li foil as anodes. The electrochemical tests of these cells were implemented using a NEWARE system (0.005-1.5 V, CT-4008T-5 V 10 mA) at 30 °C. And the cells were charge/discharge at 0.1 C (1 C = 650 mA g^{-1}) in the first two pre-cycles, then held long-cycle rate at 0.5 C.

The electrolyte injection for the NCM811/SiO_x-Gr pouch cells was conducted in a dry room to minimize the impact of H_2O on the cycling stability. These pouch cells were designed with a nominal capacity of 3.2 Ah, achieving a capacity density of up to 300 Wh kg^{-1}. The electrolyte was injected at a standard of 3 g Ah^{-1}, after which the cells are placed in a vacuum resting chamber (Shanghai Kinco Co., Ltd.) to ensure complete wetting of the electrodes and separator by the electrolyte. Subsequently, the pouch cells were pre-sealed using a vacuum packaging machine (Shanghai Kinco Co., Ltd.), and clamped with a plate to rest at room temperature for 24 h. Pre-cycling test was conducted on the pouch cells using a NEWARE test system (CT-4008T-5V 6A) at 50 °C. After two cycles, the cells were disassembled, excess electrolyte was removed, and the cells were resealed using a secondary packaging machine (Xiamen TOB New Energy Technology Co., Ltd.). Subsequently, the long-term cycling test was performed at 50 °C using a NEWARE test system with a current of 3 A.

Characterization

To confirm the successful synthesis of LiBTCB, the obtained LiBTCB power was studied by nuclear magnetic resonance (NMR, Bruker AV400 spectrometer) and high resolution mass spectrum (HRMS, Waters Xevo G2-S QToF MS/MS Spectrometer). The cycled electrodes for analysis of the surface chemistry and morphology were

obtained from the cells disassembled in a glove box. 1000 ppm H_2O was added to the BE, FEC, BE + FEC, FEC + LiBTCB and BE + FEC + LiBTCB, and stored at 50 °C for 24 h to obtained by NMR. The NCM811/SiO_x-Gr full cells with fully discharged state (0% SOC) after 300 cycles were disassembled, and the cycled NCM811 cathodes and SiO_x-Gr anodes were characterized, respectively. The surface morphology of the cycled electrodes was observed using scanning electron microscope (SEM, Hitachi S-4800). The surface and cross-sectional morphology analyses of the particles were performed by IM4000 Ion Milling System. X-ray diffraction (XRD, Bruker-AXS, Rigaku Corporation) was used to test the crystal structure changes of NCM811 cathodes. The scanning transmission electron microscopy (STEM, Thermo Fisher Titan Themis G2 60-300) was used to observe the structural evolution of cycled NCM811 cathodes prepared by focused ion beam (FIB). X-ray photoelectron spectroscopy (XPS, Thermo Scientific ESCA Lab 250Xi) and time-of-flight secondary ion mass spectrometry (ToF-SIMS, PHI nanoTOF II, ULVAC-PHI.INC) were uesd to characterize the interphase chemistry of the cycled NCM811 cathodes and SiO_x-Gr anodes. Thermal runaway was determined by accelerating rate calorimeter (ARC, BTC-130) from 60 to 500 °C. The cycled NCM811 cathodes were washed three times with EMC and then placed in the corresponding electrolytes and stored at 50 °C for 24 h to determine the TMs dissolution by inductively coupled plasma optical emission spectrometry (ICP-OES, Aglient 7850). The atomic force microscopy (AFM, Bruker Corp., Dimension Icon) was employed to collect the Young's modulus of the cycled SiO_x-Gr anodes and NCM811 cathodes. BE + FEC and BE + FEC + LiBTCB were stored in a constant temperature oven at 50 °C for 15 days, and the pH of the fresh and long-term stored electrolytes was measured using a pH meter (FiveEasy Plus, METTLER TOLEDO). For the liquid chromatography-quadrupole time-of-flight tandem mass spectrometry (LC-QTOF-MS), the cycled NCM811 cathodes were disassembled from NCM811/SiO_x-Gr full cells using BE + FEC and BE + FEC + LiBTCB, then subjected to the following treatment: First, the samples were rinsed three times with EMC to remove residual electrolyte; Subsequently, the NCM811 cathodes were individually immersed in dimethyl sulfoxide (DMSO) for 24 hours. The LC and QTOF-MS analysis of the NCM811 cathode

interphases were performed on Agilent 1290 UPLC and Agilent 6550 QTOF system (Agilent Technologies). Reversed-phase chromatography was performed using Agilent Poroshell waters BEH C18 (2.1 mm × 100 mm, 1.7 μm) and a flow rate of 0.3 ml min^{-1}. The mobile phase gradient consisted of water containing 0.1% formic acid (A) and methanol solution (B). To separate more components, the gradient was set as follows: 0-1 min 95 % A; 1-8 min 95-5 % A; 8-13 min 5 % A; 13-14 min 5-95 % A; 14-15 min 95 % A. The data acquisition was performed on a 6550 QTOF mass spectrometer equipped with a dual electrospray ion (ESI) source. The LC and QTOF-MS analysis of the fresh electrolytes and stored at 50 °C for 24 and 48 h, respectively, were performed on Bruker MaXis UHR-TOF (ultra-high resolution time-of-flight) (Bruker Daltonics Inc., Billerica, MA) at a flow rate of 0.2 mL min^{-1}. The mobile phase gradient consisted of water containing 0.1% formic acid (A) and methanol solution (B). To separate more components, the gradient was set as follows: 0-2 min 95 % A; 2-18 min 95-5 % A; 18-28 min 5 % A; 28-29 min 5-95 % A; 29-35 min 95 % A.

Theoretical calculations

Adsorption energy

The first-principles calculations[1, 2] based on density functional theory (DFT) were employed to investigate the system using the generalized gradient approximation (GGA) with the Perdew-Burke-Ernzerhof (PBE)[3] formulation. The projected augmented wave (PAW) potentials[4, 5] were used to account for ionic cores and valence electrons and a plane wave basis set with a kinetic energy cutoff of 450 eV. Partial occupancies of the Kohn-Sham orbitals were allowed using the Gaussian smearing method with a width of 0.05 eV. To optimize geometry and lattice size, Brillouin zone integration was performed with a 0.04 k-mesh Monkhorst-Pack sampling[6]. The self-consistent calculations were applied to a convergence energy threshold of 10^{-5} eV. And equilibrium geometries and lattice constants were optimized by applying maximum stress on each atom within 0.02 eV $Å^{-1}$. Additionally, a 15 Å vacuum layer was included to eliminate artificial interactions between periodic images. The weak interaction was

described using the DFT+D3 method with empirical correction in Grimme's scheme[7, 8]. Finally, the spin polarization method was used to describe the magnetic system. To calculate the adsorption energies (E_{Ads}) of $BTCB^-$, PF_6^-, EC, FEC and EMC on NCM811 surface, the following formula was used:

$$E_{ads} = E_{total} - E_{Slab} - E_X$$

Where E_{Total}, E_{Slab} and E_X represents the total energy of the system, energy of a A slab, and energy of single anion or single solvent molecule ($BTCB^-$, PF_6^-, EC, FEC or EMC).

Binding energy

The geometry of all molecules was optimized by density functional theory (DFT). All the DFT computations were performed by the M06-2X density functional method[9]. The def2-SVP[10] basis set was used for geometry optimization. All structures were generated using CYLview. The def2-TZVP[11] basis set was used for single point energy calculation. The SMD solvation model[12] was used to account for the effects of water solution. All these calculations were performed with Gaussian 16 software package.

When calculating the binding energy between other components in the electrolyte and PF_5 molecules, all calculations were carried out with the Gaussian 16 software. Geometric optimization is calculated using PBE0 functional[13], def2tsvp basis set[10] combined with D3 dispersion correction[8].

Dissociation energy

All calculations were carried out with the Gaussian 16 software. Geometry optimizations were calculated using PBE0 functional, def2tsvp basis set combined with D3 dispersion correction, in conjunction with the SMD continuum method.

Machine learning assisted screening of cyano-enriched additives

1. Data set construction and pre-processing

To establish a robust chemical space for electrolyte additive discovery, we constructed an initial ultra-large molecular library comprising **1,446,718** unique structures. This dataset was amalgamated from the open-source chemical repository, PubChem, via a targeted retrieval using the specific Boolean query "carbonitrile OR dicarbonitrile OR tricarbonitrile OR tetracarbonitrile OR pentacarbonitrile OR hexacarbonitrile OR heptacarbonitrile OR octacarbonitrile OR nonacarbonitrile OR decacarbonitrile" and supplemented with 200 proprietary structures from our in-house database designed to capture specific motifs. Given the stringent stability requirements of long-cycle-life lithium-ion batteries, a rigorous multi-stage filtration protocol was implemented using the RDKit cheminformatics toolkit:

(1) Desalting and standardization: All molecules were processed via the Salt Remover module to strip inorganic counterions (e.g., Li^+), retaining only the largest organic fragment to focus on the active anion or neutral species.

(2) Elemental and weight constraints: The allowed elemental composition was strictly limited to {*H, Li, B, C, N, O, F, Al, Si, P, S*} to avoid heavy metals or redox-unstable elements. The molecular weight (*MW*) window was set to $60 \leq MW \leq 650$ Da to balance volatility and viscosity.

(3) Aprotic structural filter: A blacklist based on SMARTS pattern matching was applied to exclude molecules containing labile protons (e.g., hydroxyls ([O;H1]), thiols ([S;H1]), primary/secondary amines ([#7;!H0])) and thermodynamically unstable linkages (e.g., peroxides (O-O), azo (N=N), and alkynes (C#C)).

(4) Functional density threshold: To ensure high electrochemical efficacy per unit mass, we imposed a functional density constraint requiring the ratio of heteroatoms to heavy atoms to exceed 0.35 ($N_{hetero}/N_{heavy} \geq 0.35$).

(5) Active motif requirement: Candidates were required to contain at least two instances of whitelist substructures (e.g., nitrile (C#N), isocyanate (N=C=O), or fluorinated/oxygenated P/Si centers) to guarantee minimal functionality.

Following this rigorous sanitization, 21,931 high-quality precursor candidates were retained for feature engineering.

2. Physics-informed feature engineering

Unlike traditional approaches that rely on generic descriptors (e.g., LogP, molecular refractivity), we developed a custom scoring engine based on three mechanism-driven descriptors (M_1, M_2, M_3) to explicitly quantify the targeted electrochemical functionalities.

Hydrophilic Scavenging Efficiency (M_1): To strictly quantify the capability of candidate molecules to mitigate electrolyte contamination, we formulated the M_1. This mechanism-driven metric evaluates a molecule's dual capacity to physically attract and chemically fixate polar impurities (both H_2O and HF), defined as:

$$M_1 = \frac{TPSA}{MW} \times 100 \times \delta_{chem}$$

Where Topological Polar Surface Area (*TPSA*) serves as a geometric proxy for the abundance of physical adsorption sites available to attract polar species via hydrogen bonding. To ensure high gravimetric efficiency, the *TPSA* is normalized by the molecular weight (*MW*). Crucially, the term δ_{chem} represents a chemical reactivity coefficient grounded in Hard-Soft Acid-Base (HSAB) theory. Molecules containing Lewis acidic centers (e.g., *B, Al, Si, P*) are assigned a high activity score ($\delta_{chem} = 1.0$) because they function as hard acids capable of forming stable coordination complexes with hard bases (e.g., the O^{2-} in H_2O or F^- in HF). Conversely, pure organic structures relying solely on reversible physical adsorption are penalized ($\delta_{chem} = 0.2$). This design prioritizes candidates that offer thermodynamic permanence in impurity removal via chemisorption, rather than transient physisorption.

Effective Lewis Basicity (M_2): This descriptor quantifies the capability of candidates to complex the aggressive Lewis acid PF_5, thereby suppressing the ring-opening polymerization of cyclic carbonates such as FEC. The binding affinity is modeled as a synergy between electronic density and steric accessibility, defined as:

$$M_2 = \frac{\sum_{i \in Atoms}\left(V_{hybird,i} + |\overline{q_i}|\right)}{MW} \times 100$$

Where $|\overline{q_i}|$ represents the magnitude of the Gasteiger partial negative charge, serving as a proxy for the local electron density available for donation. Crucially, the term $V_{hybird,i}$ encodes the orbital geometry of the donor sites. Atoms with *sp*-hybridization (e.g., nitrogen in cyano groups) are assigned a high structural reward (*V*

= *1.0*). This reflects the directional nature of *sp* lone pairs and the linear geometry of the cyano group, which minimizes steric hindrance and facilitates the approach of the bulky PF_5 molecule. Conversely, donor atoms (e.g., oxygen) adjacent to internal Lewis acidic centers (e.g., *B, Al, Si,* and *P*) are penalized (*V = 0.5*) to account for the reduced nucleophilicity caused by *p-π* back-bonding, which delocalizes the lone pair electrons and weakens external complexation capability.

Synthetic Feasibility (M_3): We utilized topological symmetry as a proxy for structural stability and synthesis ease. High symmetry often correlates with reduced information entropy and simplified synthetic routes:

$$M_3 = \frac{N_{atoms}}{N_{unique\_ranks} + 1}$$

Where N_{atoms} is the total atom count and N_{unique_ranks} is the number of topologically unique atoms derived from Canonical Ranking. A higher M_3 score indicates a molecule with high structural degeneracy (e.g., C_2 or C_3 rotation axes). From a synthetic perspective, this suggests that the target molecule can likely be assembled via modular "one-pot" reactions (e.g., attaching identical ligands to a central core) rather than complex and multi-step sequential synthesis. This significantly lowers the barrier for purification and scalable manufacturing by minimizing the complexity penalty associated with asymmetric organic synthesis.

3. Unsupervised clustering and rank mapping

To deconvolute the high-dimensional complexity of the screened library and identify structurally distinct molecular families, we implemented a multi-stage unsupervised machine learning protocol.

Manifold learning & dimensionality reduction: Instead of relying on linear projections (e.g., Principal Component Analysis (PCA)) which often fail to capture non-linear chemical relationships, we utilized Uniform Manifold Approximation and Projection (UMAP). The 1024-bit Morgan fingerprints were projected into a dense 5-dimensional latent manifold. This transformation preserves both the local topological neighborhoods and the global structural hierarchy, enabling the algorithm to cluster molecules based on functional similarity rather than just substructure matching.

Hyperparameter optimization (elbow method): To eliminate subjective bias in determining the optimal number of clusters (k), we employed a geometric curvature analysis of the K-Means inertia curve. Instead of relying on visual estimation, we calculated the orthogonal Euclidean distance from each data point on the inertia curve to the chord line connecting the extremities of the curve (k_{min} *to* k_{max}). The value k maximizing this distance represents the point of diminishing returns. Based on this rigorous mathematical criterion, the chemical space was optimally partitioned into $k = 8$ distinct clusters.

Performance-based rank mapping: Post-clustering, we established a bridge between unsupervised structural grouping and physics-informed performance. A total score S was calculated for each molecule using a weighted linear combination:

$$S_{total} = 0.4 \times M_{1,norm} + 0.4 \times M_{2,norm} + 0.2 \times M_{3,norm}$$

Clusters were then re-indexed based on their mean group scores. This Rank Mapping protocol automatically identifies the elite cluster (*Cluster 0*) that statistically enriches the desired physicochemical attributes, guiding experimentalists toward the most promising chemical subspace.

4. Candidate prioritization and structural reconstruction

The final stage involved the precise selection and chemical reconstruction of top-tier candidates for experimental validation.

Automated charge neutralization (re-lithiation protocol): Since inorganic counterions were intentionally stripped during the initial desalting stage to isolate the active organic fragments for descriptor calculation, we developed an automated re-lithiation algorithm to restore the full salt structure. For every anionic candidate identified in the top tier, the algorithm computes the formal charge and stoichiometrically appends charge-balancing lithium cations (Li^+) to generate the neutral salt formula (e.g., converting $BTCB^-$ back to LiBTCB). This step is critical for ensuring stoichiometric integrity during subsequent DFT geometry optimizations and experimental synthesis.

Applying this physics-informed workflow, the initial library of 1,446,718 structures was efficiently funneled down. We prioritized the top-ranked candidates from

the elite cluster (Rank 1-10), which exhibited the optimal trade-off between scavenging capability ($\boldsymbol{M_1}$), Lewis basicity ($\boldsymbol{M_2}$), and synthetic accessibility ($\boldsymbol{M_3}$). This data-driven pipeline effectively bypasses the traditional "trial-and-error" bottleneck, delivering high-probability targets for preserving the cycling stability of LIBs at elevated temperatures.

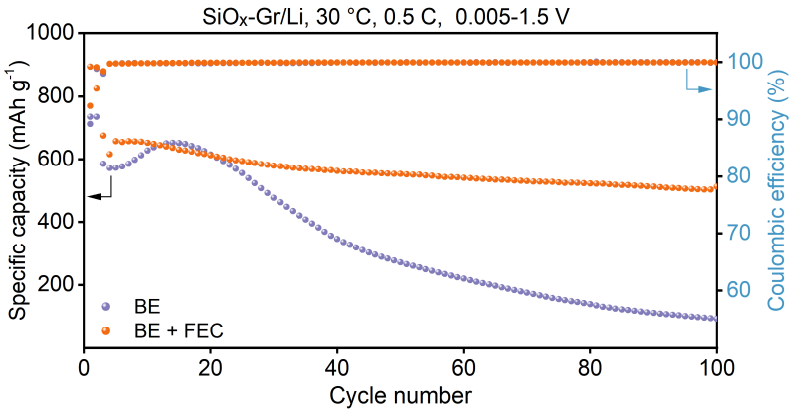

Figure S1. Cycling performance of SiO_x-Gr/Li half cells using BE and BE + FEC at 30 °C.

Compared with the BE counterpart (15.63% retention, 91.48 mAh g^{-1}/585.23 mAh g^{-1}, average Coulombic efficiency (ACE) = 99.28%, 100th cycle), the capacity retention of the SiO_x-Gr/Li half cell using BE + 10 wt.% FEC increases to 75.94% (512.84 mAh g^{-1}/675.33 mAh g^{-1}, ACE =99.92%).

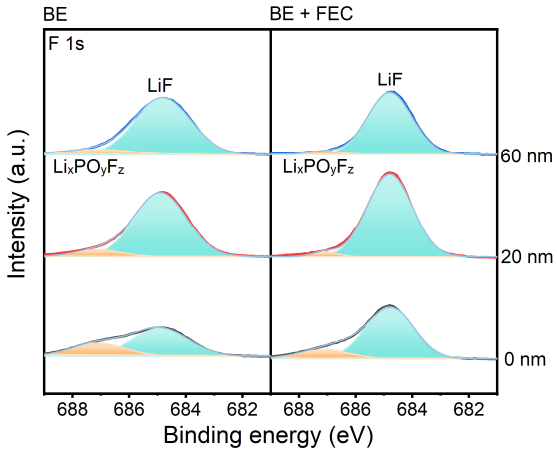

Figure S2. F 1s *in-depth* XPS of cycled SiO_x-Gr anodes using BE and BE + FEC at 30 ℃.

The F 1s *in-depth* XPS spectrum reveals the enhanced formation of LiF (ca. 684.8 eV) by the FEC additive. Additionally, the FEC contributes to the suppression of $LiPF_6$ decomposition, as evidenced by the reduction of $Li_xPO_yF_z$ species (ca. 687.2 eV).

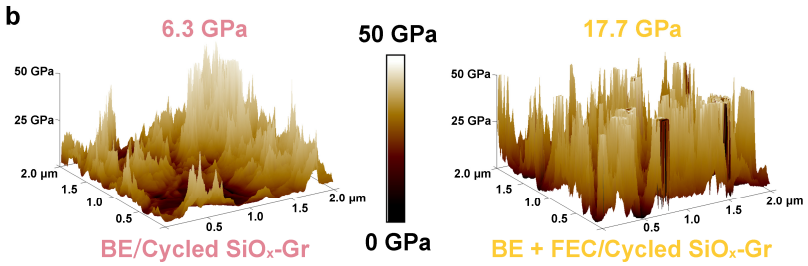

Figure S3. Modulus mappings of cycled SiO_x-Gr anodes disassembled from SiO_x-Gr/Li half cells using BE and BE + FEC at 30 ℃.

The Young's modulus of SEI layer on SiO_x-Gr anodes is increased from 6.3 to 17.7 GPa by FEC additive.

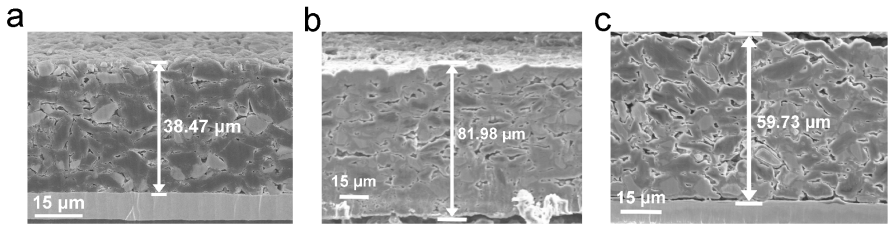

Figure S4. Cross-sectional SEM images for the (a) pristine and cycled SiO_x-Gr anode disassembled from SiO_x-Gr/Li half cell using (b) BE and (c) BE + FEC at 30 °C.

Typical cross-section SEM is used to visually examine the volume expansion of the SiO_x-Gr anodes at 30 °C. The thickness of the cycled SiO_x-Gr anode using BE increases dramatically from the initial 38.47 µm to 81.98 µm, corresponding to a volume expansion of 213%. However, upon the addition of 10 wt.% FEC, the volume expansion of the anode is significantly mitigated, with the thickness reduced to 59.73 µm and the volume expansion limited to 155%.

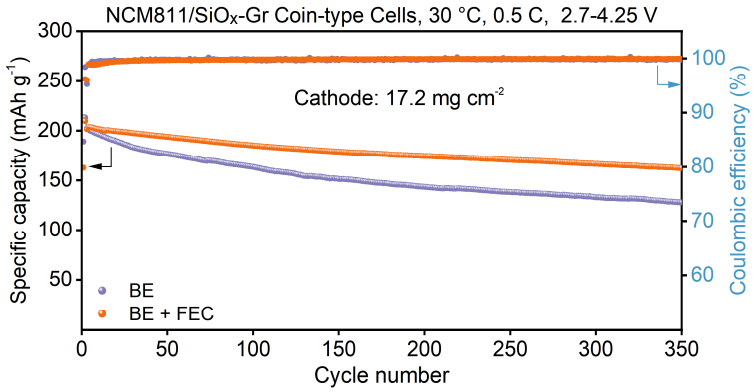

Figure S5. Cycling performance of NCM811/SiO_x-Gr full cells using BE and BE + FEC at 30 °C.

At 30 °C, the addition of FEC enhances the cycle stability of NCM811/SiO_x-Gr full cells, and the capacity retention increases from 63.07% (127.67 mAh g^{-1}/202.41 mAh g^{-1}) to 80.52% (162.15 mAh g^{-1}/201.38 mAh g^{-1}) after 350 cycles.

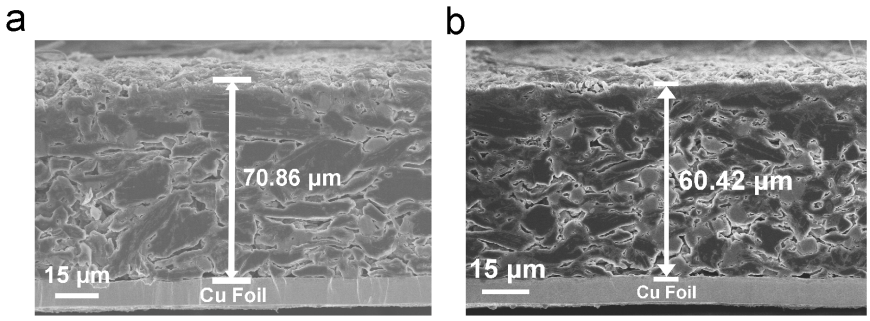

Figure S6. Cross-sectional SEM images for the cycled SiO_x-Gr anode disassembled from NCM811/SiO_x-Gr full cell using (a) BE and (b) BE + FEC at 50°C.

Typical cross-section SEM is used to visually examine the volume expansion of the SiO_x-Gr anodes cycled in the NCM811/SiO_x-Gr full cells at 50°C. The results demonstrate that the thickness of the cycled SiO_x-Gr anode with BE expands sharply from the initial 38.47 μm to 70.86 μm, resulting in a volume expansion of 184%. In contrast, the addition of 10 wt.% FEC significantly mitigates the volume expansion of the anode, with a final thickness of 60.42 μm and the volume expansion limited to 157%.

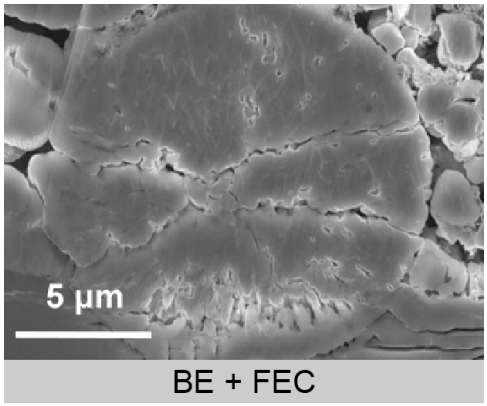

Figure S7. Cross-sectional SEM images for the cycled NCM811 cathode disassembled from NCM811/SiO_x-Gr full cells using BE + FEC at 50 °C.

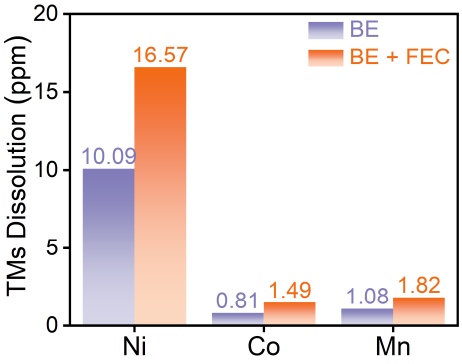

Figure S8. TMs dissolution from fully delithiated NCM811 cathode disassembled from NCM811/SiO_x-Gr full cells using BE and BE + FEC at 50 °C.

Inductively coupled plasma mass spectrometry (ICP-MS) reveals that the addition of FEC additive accelerates the TMs dissolution at 50 °C, as evidenced by the increased concentrations (ppm) of Ni, Co, and Mn increasing from 10.09, 0.81, and 1.08 to 16.57, 1.49, and 1.82, respectively.

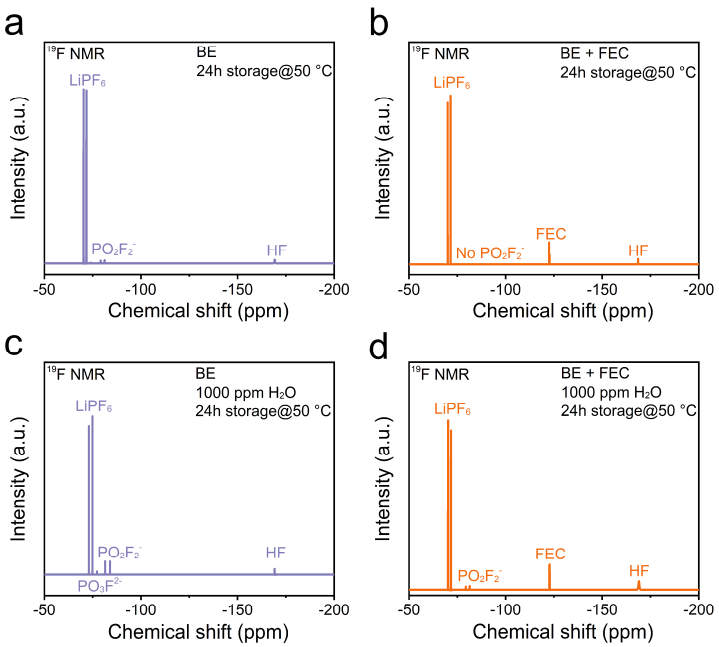

Figure S9. ^{19}F NMR spectra of (a) BE, (b) BE + FEC, (c) BE containing 1000 ppm H_2O, and (d) BE + FEC containing 1000 ppm H_2O after storage 24h at 50 °C.

In the BE electrolyte, $LiPF_6$ undergoes hydrolysis with trace residual H_2O at 50 °C, producing a HF signal at -167.8 ppm along with a distinct $PO_2F_2^-$ resonance (ca. -80 ppm). In BE + FEC electrolyte, the HF signal markedly intensifies, whereas the $PO_2F_2^-$ peak disappears, indicating that trace H_2O preferentially reacts with FEC rather than with $LiPF_6$ at 50 °C. Furthermore, it is indicated that the deliberate addition of 1000 ppm H_2O significantly accelerates the hydrolysis of $LiPF_6$ in the BE electrolyte, as evidenced by the pronounced increase of the characteristic HF peak at -167.8 ppm, along with the emergence of the $PO_2F_2^-$ resonance and further hydrolysis product PO_3F^{2-} (ca. -77 ppm). In contrast, in the BE + FEC electrolyte, although the introduction of H_2O also promotes hydrolysis, the signals corresponding to $LiPF_6$ hydrolysis products are notably weaker than in BE, whereas the HF peak is substantially enhanced. These observations further confirm that FEC preferentially reacts with trace H_2O over $LiPF_6$, generating a large amount of corrosive HF and thereby posing a risk to high-nickel cathodes.

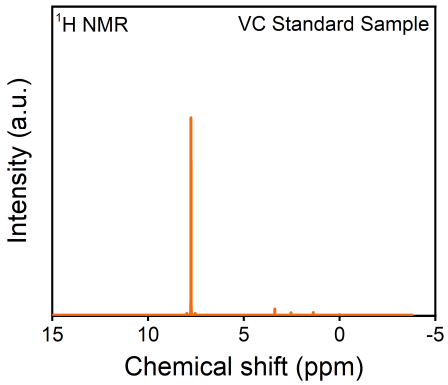

Figure S10. ^{1}H NMR spectra of VC Standard Sample.

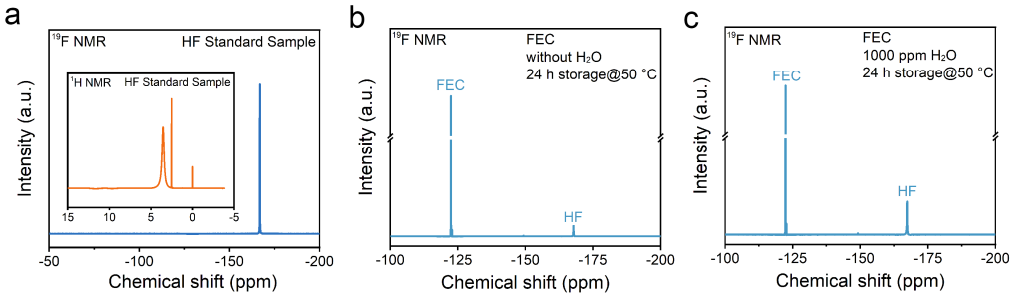

Figure S11. (a) ^{19}F NMR spectra of HF Standard Sample (the insert is ^{1}H NMR spectra of HF Standard Sample). ^{19}F NMR spectra of (b) sole FEC without H_2O and (c) FEC containing 1000 ppm H_2O after storage 24h at 50 °C.

To investigate the elevated temperature decomposition process of FEC, 1000 ppm H_2O is added to FEC, then stored at 50 °C for 24 h prior to conducting ^{19}F NMR. Characteristic peaks corresponding to HF (ca. -167.8 ppm, ^{19}F NMR) are enhanced by adding H_2O into FEC.

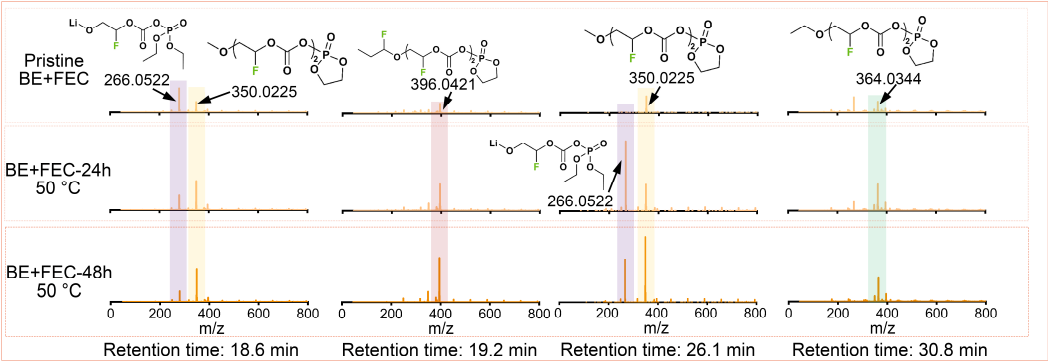

Figure S12. Mass spectra of 50 °C stored BE + FEC electrolytes at corresponding chromatographic retention times.

In the BE + FEC electrolyte, the polymerization products observed at different retention times mainly result from PF_5-catalyzed ring-opening polymerization of FEC. The accumulation of these polymeric species reflects the continuous electrolyte decompositions and increased viscosity during thermal aging.

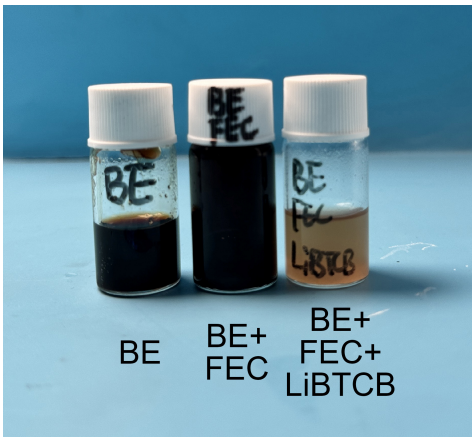

Figure S13 Digital photo of different electrolytes after storage at 50 °C for 15 days.

After 50 °C storage for 15 days, the BE electrolyte exhibited a noticeably darker color, indicating severe decomposition and degradation of the electrolyte. In contrast, the BE + FEC electrolyte not only showed significant darkening but also displayed pronounced wall-adhering behavior, suggesting a drastic increase in viscosity. This phenomenon is primarily attributed to the PF_5-induced ring-opening polymerization of FEC, leading to the formation of numerous high-molecular-weight oligomeric species. In comparison, the BE + FEC + LiBTCB electrolyte showed no obvious change in viscosity, and its color only slightly deepened after thermal storage, implying effectively suppressed polymerization and improved thermal stability.

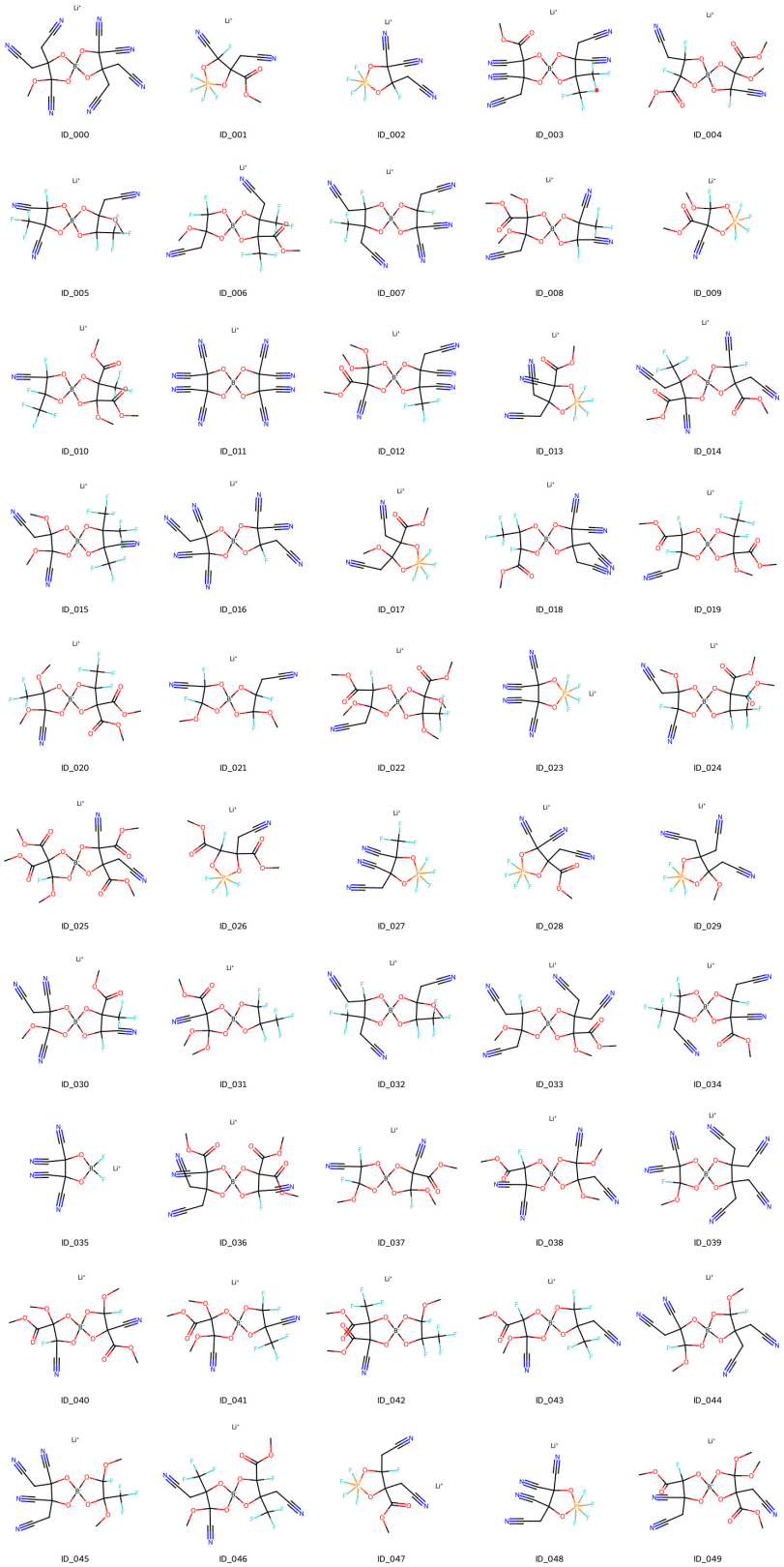

Figure S14. Proprietary structures from our in-house database (ID_000 to ID_049).

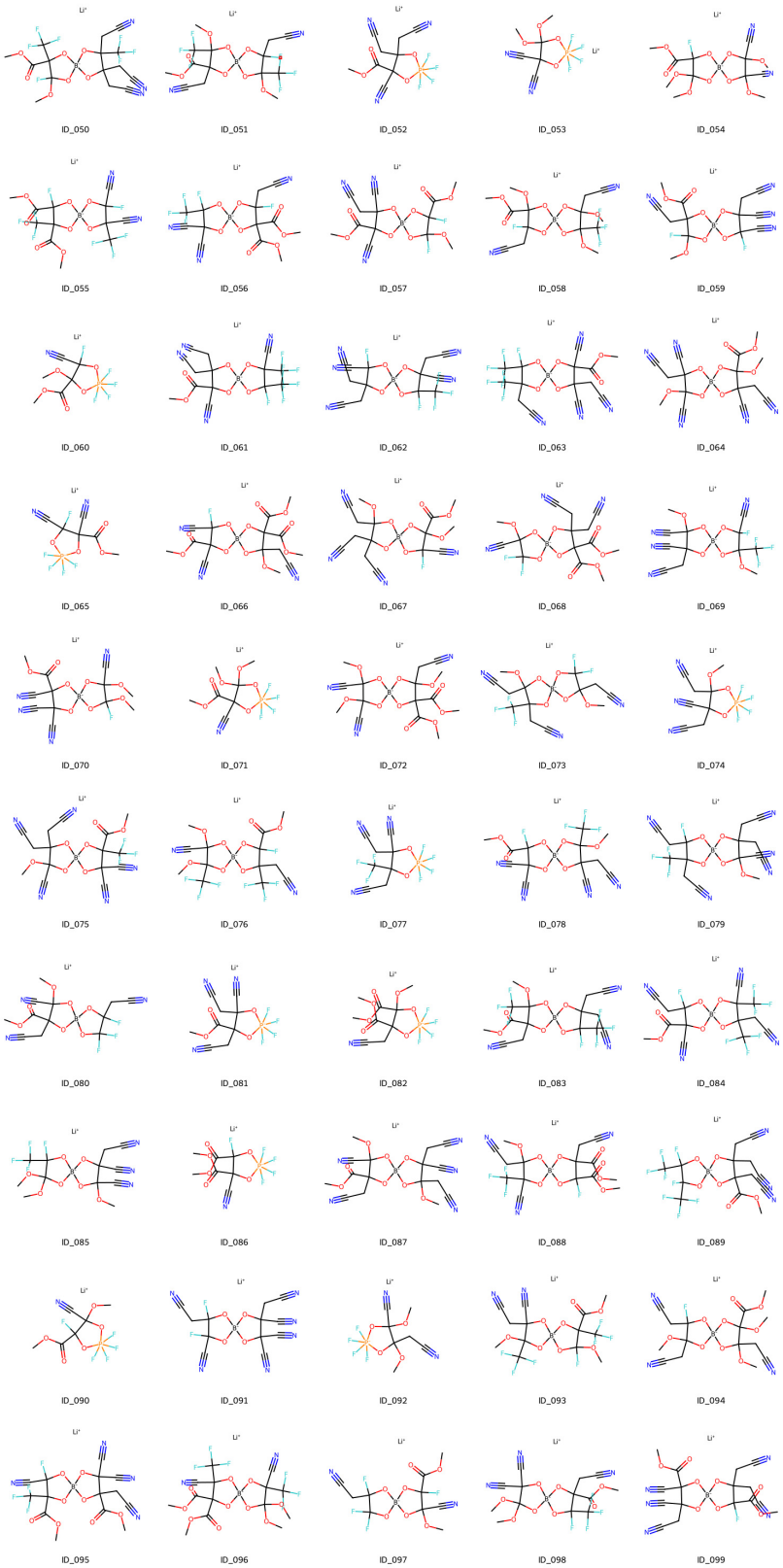

Figure S15. Proprietary structures from our in-house database (ID_050 to ID_099).

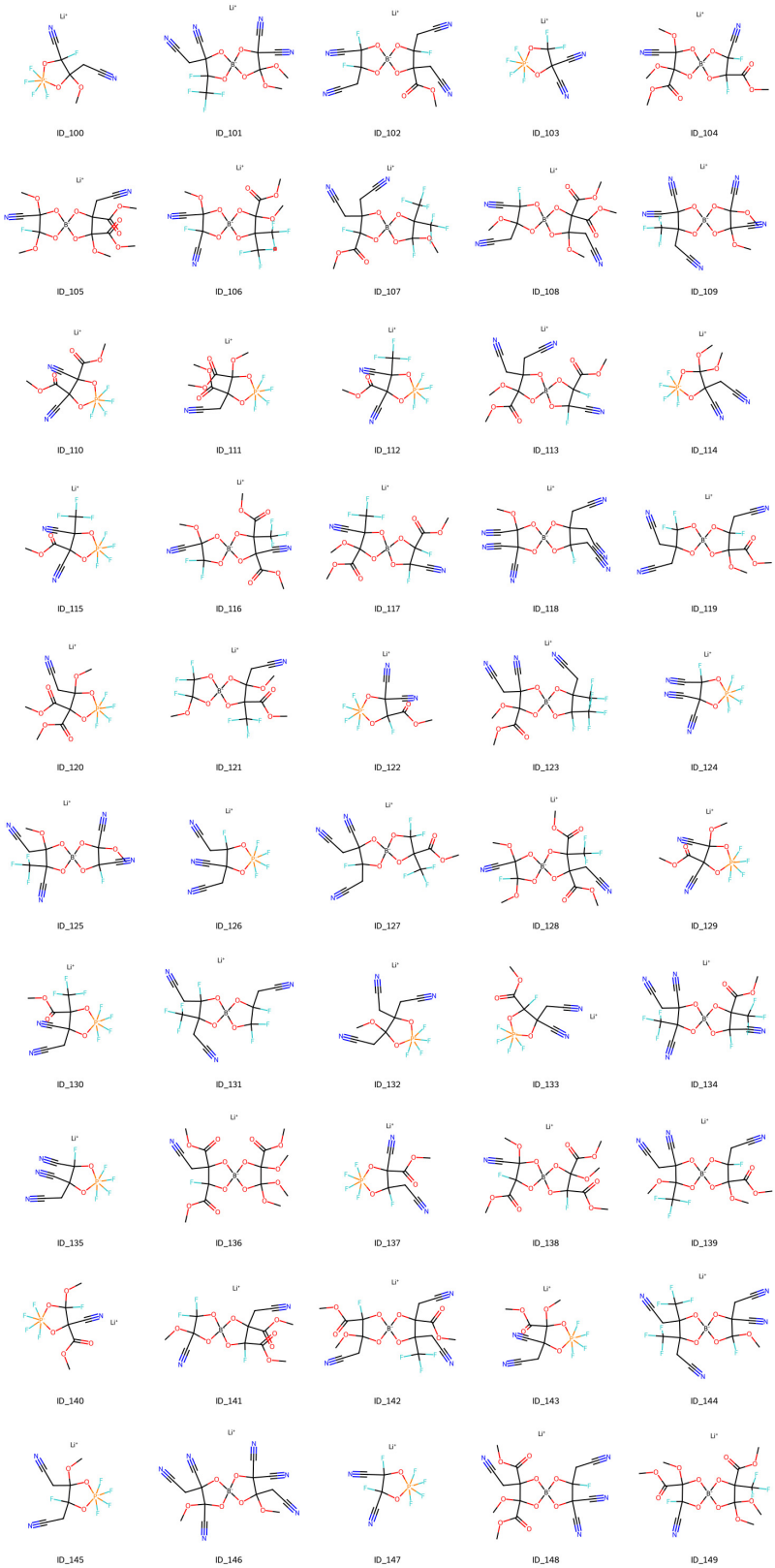

Figure S16. Proprietary structures from our in-house database (ID_100 to ID_149).

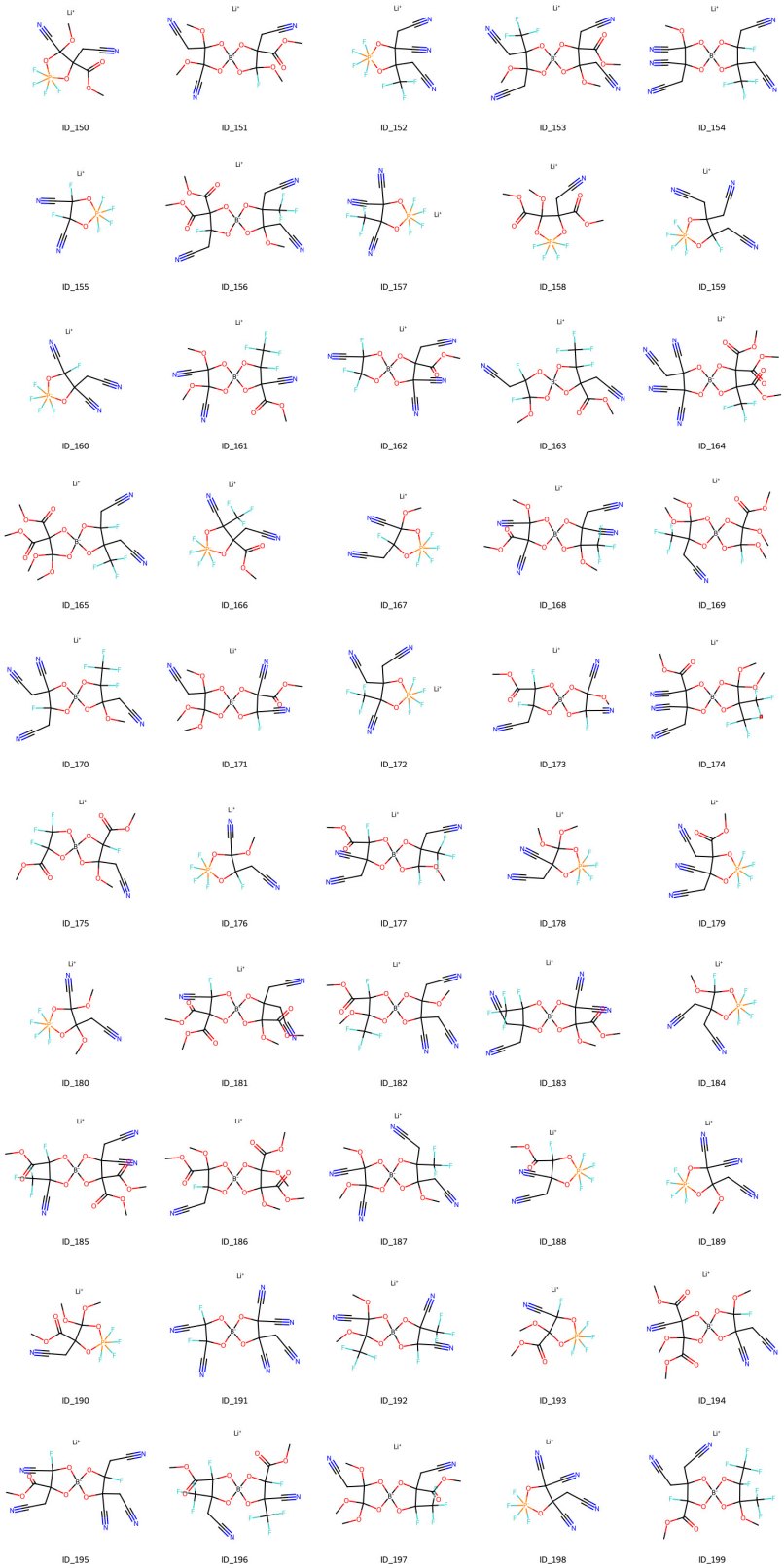

Figure S17. Proprietary structures from our in-house database (ID_150 to ID_199).

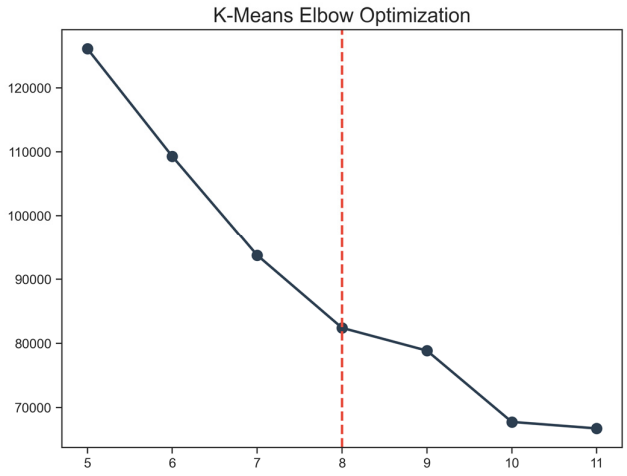

Figure S18. Determination of the optimal number of clusters (*k*) via the geometric Elbow Method.

The plot illustrates the Sum of Squared Errors (SSE) decay curve (blue line) relative to the number of clusters. The optimal value, *k=8*, is identified as the point exhibiting the maximum orthogonal distance to the chord line (red dashed line) connecting the curve endpoints (*k=5* and *k=11*).

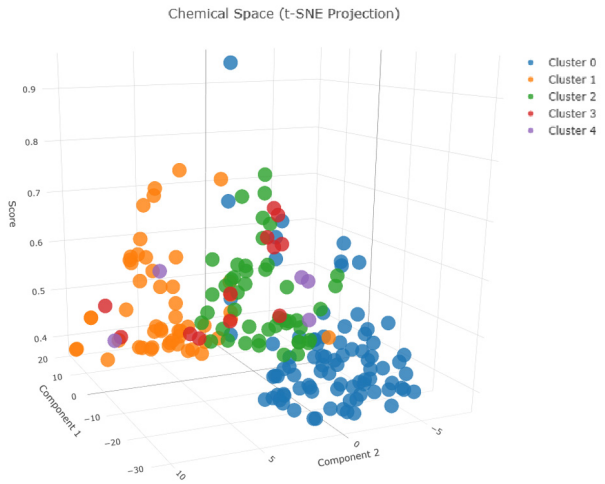

Dashboard_Interactive.html

Figure S19. Three-dimensional projection of the chemical space landscape for the top 200 elite candidates.

The 3D scatter plot exclusively maps the distribution of the highest-ranked molecules (Rank 1 to 200) onto a low-dimensional manifold derived from t-Distributed Stochastic Neighbor Embedding (t-SNE). The first two dimensions represent structural similarity on the horizontal plane, while the weighted total score is plotted along the Z-axis to visualize the performance apex. Candidates are color-coded according to their structural families identified via K-means clustering.

Note: An interactive version of this 3D model is provided as an embedded HTML file (Dashboard_Interactive.html), enabling dynamic manipulation and point-specific structural inspection for these elite data points.

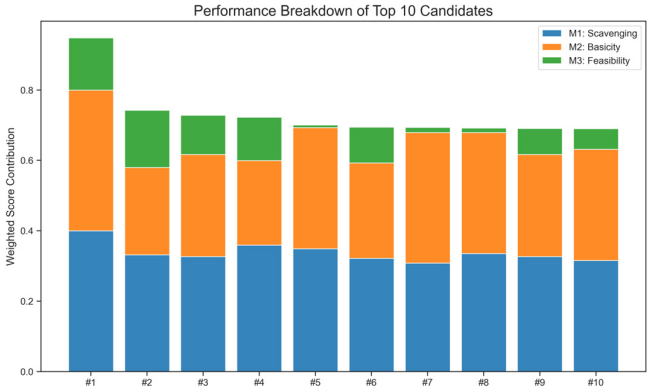

Figure S20. Component analysis of the weighted aggregate scores for the top 10 ranked candidates.

The stacked bar chart decomposes the total score into its constituent physicochemical descriptors: Hydrophilic Scavenging Efficiency (M_1, blue), Effective Lewis Basicity (M_2, orange), and Synthetic Feasibility (M_3, green). The height of each bar represents the final weighted score, validating the efficacy of the scoring engine in prioritizing thermodynamic stability and impurity scavenging capabilities.

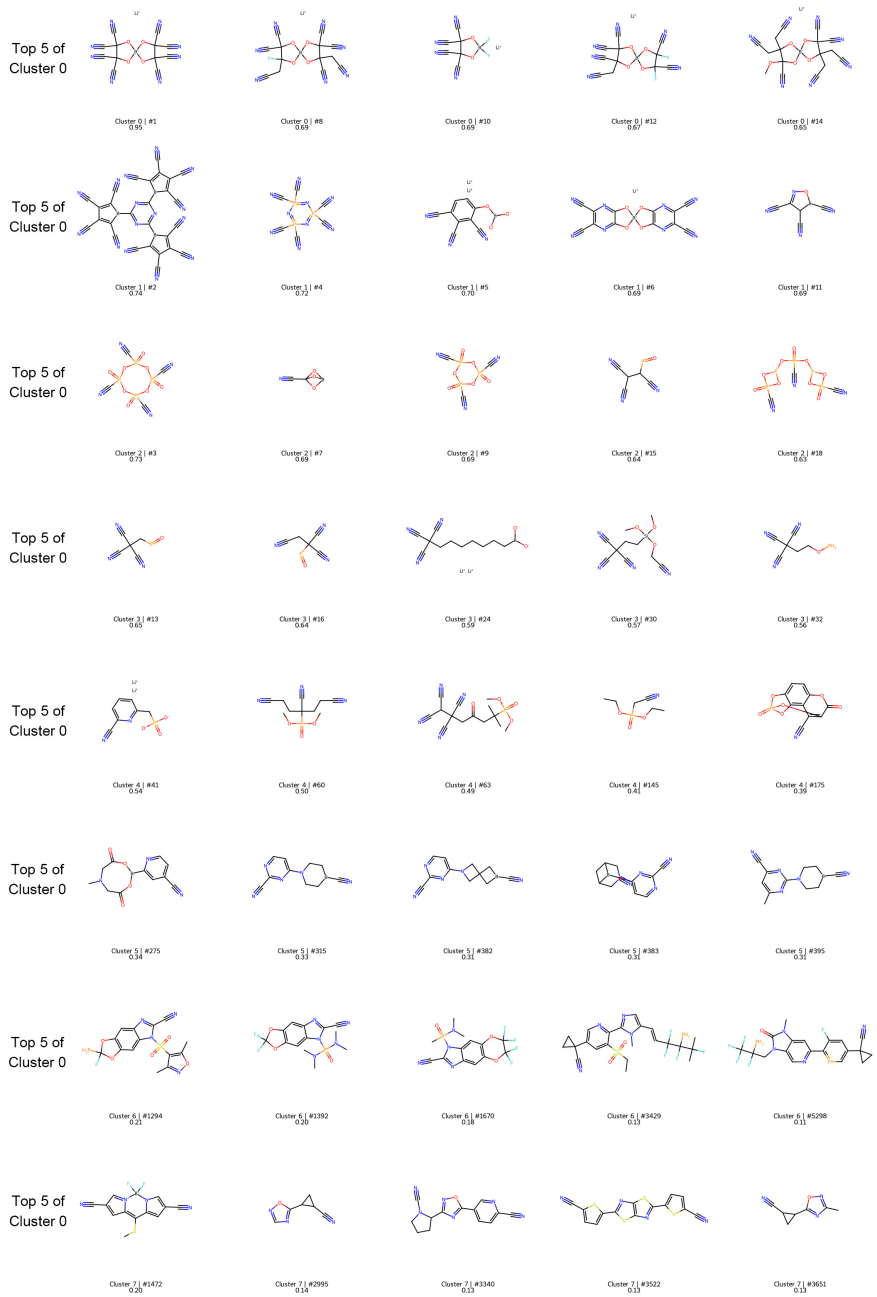

Figure S21. Representative structures of elite candidates across distinct chemical families.

This figure presents a structural matrix displaying the top 5 scoring candidates extracted from each of the clusters identified via the unsupervised learning pipeline. Rows correspond to unique structural clusters and highlight the specific molecular motifs. Each molecule is annotated with its Global Rank and Total Score, demonstrating the screening platform's capability to discover high-performance diversity beyond a single structural archetype.

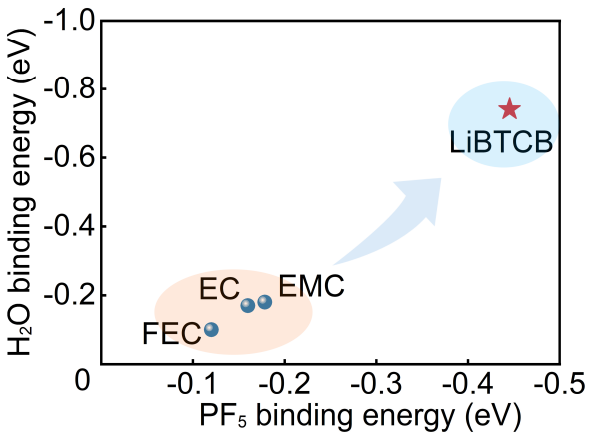

Figure S22. Binding energy of PF_5 and H_2O with different electrolyte components.

Theoretical calculations demonstrate that the top-ranked candidates identified via high-throughput screening exhibit strong binding affinity toward PF_5, thereby contributing to electrolyte stabilization during cycling. Among these electrolyte components, LiBTCB possesses the strongest binding energy with PF_5 (-0.445 eV), which accounts for the superior cycling stability observed in cells employing the BE + FEC + LiBTCB. Meanwhile, LiBTCB additive possesses the highest capability of binding H_2O (-0.74 eV), effectively inhibiting the hydrolysis of FEC and $LiPF_6$, thus blocking the generation of corrosive HF.

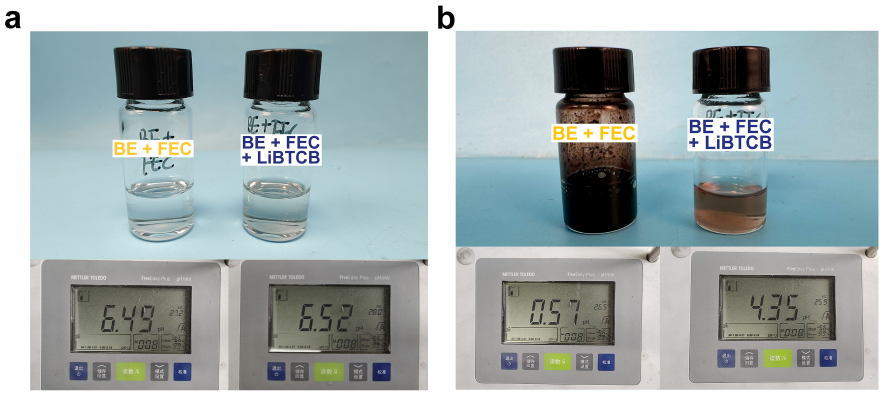

Figure S23. The corresponding pH value comparison for fresh electrolytes (a) and (b) electrolytes after storage at 50 °C for 15 days.

Fresh BE + FEC and BE + FEC + LiBTCB electrolytes are close to neutral solutions at room temperature before high-temperature storage. Afterward, the color and pH changes of various electrolytes are further tested following 15 d of storage at 50 °C. The results show that the BE + FEC sample becomes opaque extreme dark yellow color with a low pH value of 0.57, while BE + FEC + LiBTCB sample shows transparent light yellow color with a high pH value of 4.35.

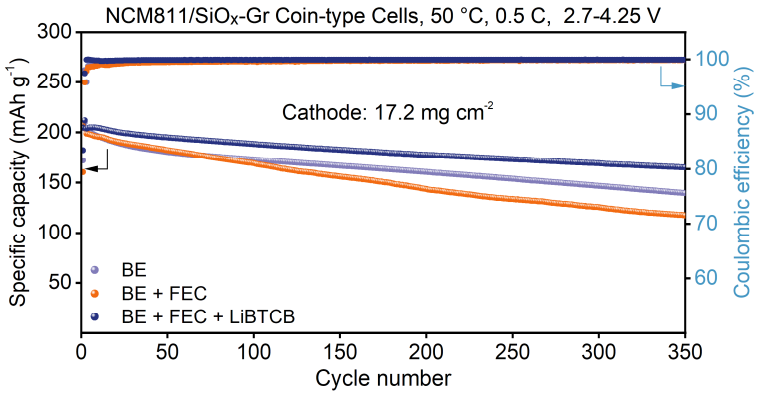

Figure S24. Cycling performance of NCM811/SiO_x-Gr full cells using BE, BE + FEC, and BE + FEC + LiBTCB at 50 ℃.

The cycling performance of NCM811/SiO_x-Gr full cell using LiBTCB (Rank 1 candidate) additive with BE + FEC is supplemented. At 0.5 C rate, the NCM811/ SiO_x-Gr full cell using BE + 10 wt.% FEC + 0.5 wt.% LiBTCB presents the best cycle life with a highest capacity retention of 81.01% (165.07 mAh g^{-1}/203.77 mAh g^{-1}, ACE = 99.86%, 350th cycle) among others. Meanwhile, the capacity retention of NCM811/SiO_x-Gr full cells using BE and BE + FEC is only 69.04% (139.53 mAh g^{-1}/202.09 mAh g^{-1}) and 59.11% (117.46 mAh g^{-1}/198.71 mAh g^{-1}), respectively.

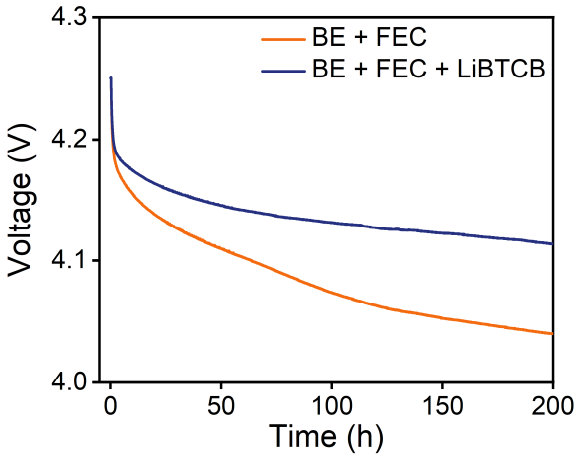

Figure S25. Representative voltage decay curve of NCM811/SiO_x-Gr full cells using different electrolytes charged to 100% SOC measured at 50 °C.

The incorporation of LiBTCB as a water scavenger effectively inhibits the hydrolysis of FEC and $LiPF_6$, thereby stabilizing the internal environment of the cells. Consequently, the self-discharge behavior of the full cell at 50 °C is significantly mitigated, as indicated by improved voltage retention (4.11 V *vs.* 4.04 V after 200 h).

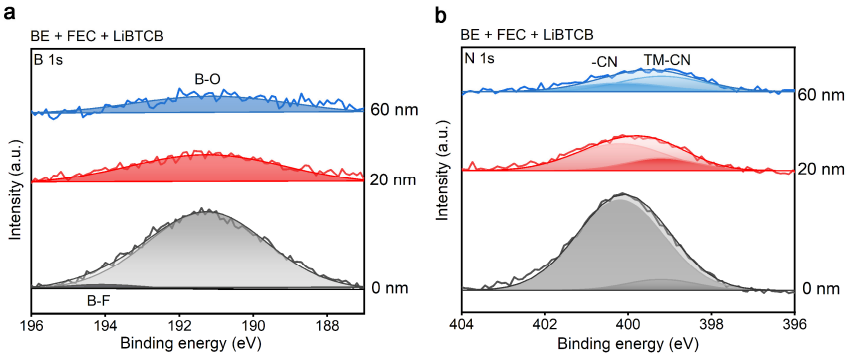

Figure S26. (a) B 1s and (b) N 1s *in-depth* XPS of cycled NCM811 cathode using BE + FEC + LiBTCB at 50 °C.

The chemical composition of CEI layer is further revealed by *in-depth* Ar^+ sputtering (0 nm, 20 nm, and 60 nm) XPS analysis. The B 1s XPS spectrum reveals a characteristic peak attributed to B-O species at ca. 191.3 eV. Additionally, the analysis demonstrates the participation of -CN groups (ca. 400.1 eV, N 1s) in the formation of the CEI layer, along with the identification of CN-TM complexation (ca. 399.2 eV, N 1s). These cyano-groups form complexes with TMs, which suppress TMs dissolution and enhance the structural stability of the NCM811 cathode.

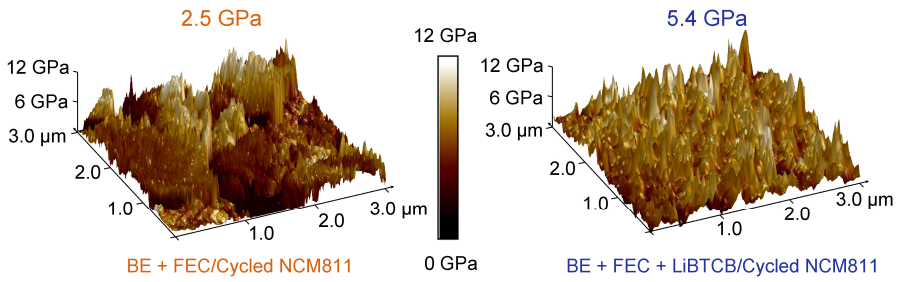

Figure S27. Modulus mappings of cycled NCM811 cathodes using BE + FEC and BE + FEC + LiBTCB.

AFM characterization demonstrates that the LiBTCB can reduce the roughness of NCM811 cathode surface and increase the Young's modulus from 2.5 GPa to 5.4 GPa.

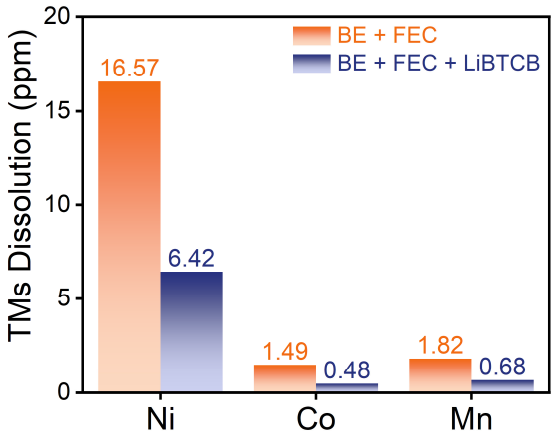

Figure S28. TMs dissolution from fully delithiated NCM811 cathodes disassembled from NCM811/SiO_x-Gr full cells using BE + FEC and BE + FEC + LiBTCB at 50 °C.

To further confirm the inhibitory effect of LiBTCB additive on the TMs dissolution of NCM811, ICP-MS is used to characterize the fully delithiated cathode. The result shows that with the help of LiBTCB additive, the contents of Ni, Co and Mn in the corresponding electrolytes are significantly reduced from 16.57, 1.49 and 1.82 ppm to 6.42, 0.48 and 0.68 ppm, respectively.

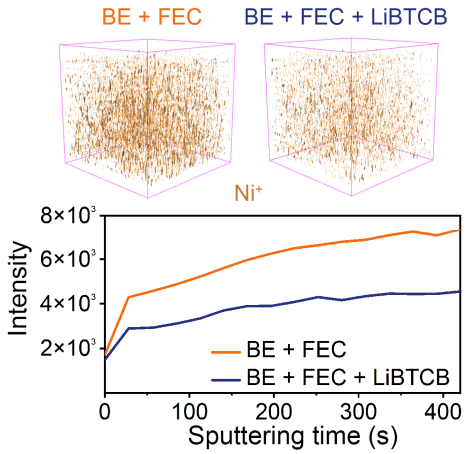

Figure S29. Ni^+ ToF-SIMS 3D reconstruction and corresponding depth profiles of cycled NCM811 cathodes using BE + FEC and BE + FEC + LiBTCB at 50 °C.

By comparing ToF-SIMS 3D element reconstruction image of NCM811 cathode, the observed Ni^+ species decrease in the CEI layer of NCM811 cathode suggests that TMs dissolution from NCM811 is greatly alleviated by LiBTCB additive.

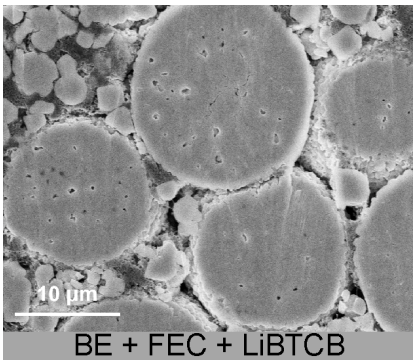

Figure S30. Cross-sectional SEM image of NCM811 cathode cycled using BE + FEC + LiBTCB at 50 °C.

The microcracking of NCM811 particles is significantly reduced by LiBTCB additive.

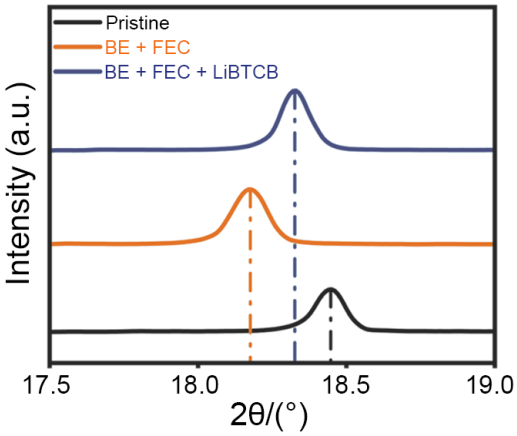

Figure S31. XRD patterns of cycled NCM811 cathodes at varied electrolytes.

As a result, X-ray diffraction (XRD) patterns clearly demonstrate that the crystal structure (the (003) peak) of cycled NCM811 cathode is well retained (less lattice expansion) with the help of LiBTCB additive.

As for the cycled SiO_x-Gr anode, ToF-SIMS analysis (Figure S32) shows that LiBTCB can also decompose on the surface of SiO_x-Gr anode to form a robust inorganic-dominated SEI enriched with BO_2^-. Similarly, characteristic peaks attributed to B-O species were also observed in B 1s *in-depth* Ar^+ sputtering XPS (Figure S33a, ca. 191.3 eV). FEC favors the enrichment of LiF species (e.g. Li_2F^+) in the SEI layer (Figure S33b, S34), as mentioned in the previous section, LiF with a high Young's modulus can effectively accommodate the volume change of SiO_x-based anodes during the process of Li^+ insertion/extraction. As expected, under the synergistic effect of LiBTCB and FEC, less C-C (ca. 284.2 eV) and C-O (ca. 286.2 eV) species indicating attenuated solvent decomposition (Figure S35, C 1s *in-depth* XPS). In summary, LiBTCB and FEC help to synergistically form a robust and robust SEI layer enriched with BO_2^- and LiF, which can effectively suppress the decomposition of electrolyte and volume change of SiO_x-Gr anode, thereby achieving commercial LIBs with long cycle stability.

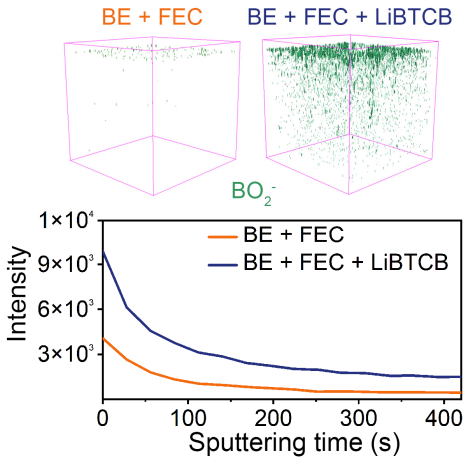

Figure S32. BO_2^- ToF-SIMS 3D reconstruction and corresponding depth profiles of cycled SiO_x-Gr anodes using BE + FEC and BE + FEC + LiBTCB at 50 °C.

ToF-SIMS analysis shows that LiBTCB can decompose on the surface of SiO_x-Gr anode to form a robust inorganic-dominated SEI enriched with BO_2^-.

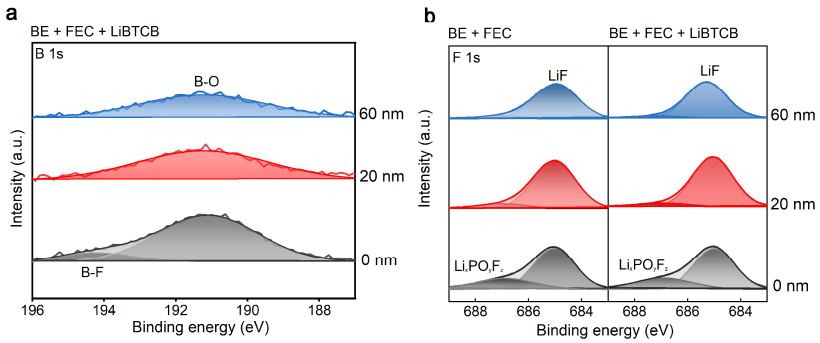

Figure S33. (a) B 1s and (b) F 1s *in-depth* XPS of cycled SiO_x-Gr anodes using BE + FEC and BE + FEC + LiBTCB at 50 °C.

The characteristic peak (ca. 191.3 eV, B 1s) attributed to the B-O species is also observed. As mentioned above, FEC is beneficial to the formation of a LiF-enriched SEI layer, which can effectively adapt to the volume change and prevent the SiO_x-Gr anode from powdering.

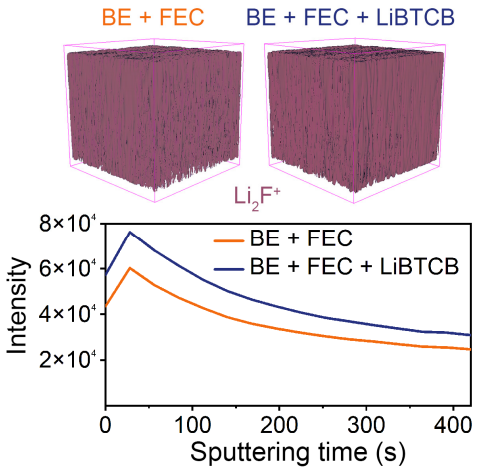

Figure S34. Li_2F^+ ToF-SIMS 3D reconstruction and corresponding depth profiles of cycled SiO_x-Gr anodes using BE + FEC and BE + FEC + LiBTCB at 50 °C.

FEC favors the enrichment of LiF species (e.g. Li_2F^+) in the SEI layer, and LiF with a high Young's modulus can effectively accommodate the volume change of SiO_x-based anodes during the process of Li^+ insertion/extraction.

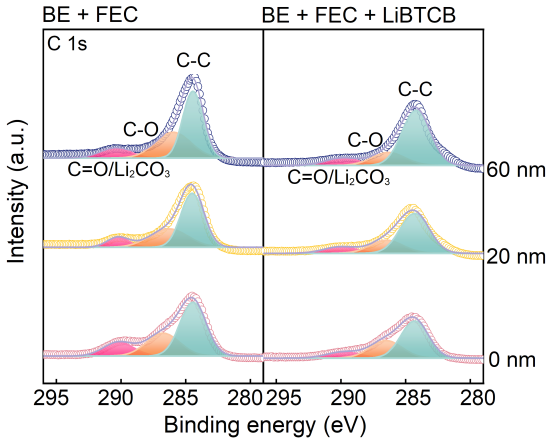

Figure S35. C 1s *in-depth* XPS of cycled SiO_x-Gr anodes using BE + FEC and BE + FEC + LiBTCB at 50 °C.

The incorporation of the LiBTCB additive reduces the presence of C-C (ca. 284.2 eV) and C-O (ca. 286.2 eV) species in the C 1s XPS spectrum, indicating that solvent reduction processes are effectively mitigated.

References

(1) Kresse, G.; Furthmüller, J. Efficiency of ab-initio total energy calculations for metals and semiconductors using a plane-wave basis set. *Computational Materials Science* **1996**, *6* (1), 15-50.

(2) Kresse, G.; Furthmüller, J. Efficient iterative schemes for ab initio total-energy calculations using a plane-wave basis set. *Physical Review B* **1996**, *54* (16), 11169-11186.

(3) Perdew, J. P.; Burke, K.; Ernzerhof, M. Generalized Gradient Approximation Made Simple. *Phys. Rev. Lett.* **1996**, *77* (18), 3865-3868.

(4) Kresse, G.; Joubert, D. From ultrasoft pseudopotentials to the projector augmented-wave method. *Physical Review B* **1999**, *59* (3), 1758-1775.

(5) Blöchl, P. E. Projector augmented-wave method. *Physical Review B* **1994**, *50* (24), 17953-17979.

(6) Monkhorst, H. J.; Pack, J. D. Special Points for Brillouin-Zone Integrations. *Physical Review B* **1976**, *13* (12), 5188-5192.

(7) Grimme, S.; Ehrlich, S.; Goerigk, L. Effect of the damping function in dispersion corrected density functional theory. *J. Comput. Chem.* **2011**, *32* (7), 1456-1465.

(8) Grimme, S.; Antony, J.; Ehrlich, S.; Krieg, H. A consistent and accurate ab initio parametrization of density functional dispersion correction (DFT-D) for the 94 elements H-Pu. *J. Chem. Phys.* **2010**, *132* (15), 154104.

(9) Adamo, C.; Barone, V. Toward reliable density functional methods without adjustable parameters: The PBE0 model. *The Journal of Chemical Physics* **1999**, *110* (13), 6158-6170.

(10) Weigend, F.; Ahlrichs, R. Balanced basis sets of split valence, triple zeta valence and quadruple zeta valence quality for H to Rn: Design and assessment of accuracy. *Phys. Chem. Chem. Phys.* **2005**, *7* (18), 3297-3305.

(11) Weigend, F. Accurate Coulomb-fitting basis sets for H to Rn. *Phys. Chem. Chem. Phys.* **2006**, *8* (9), 1057-1065.

(12) Marenich, A. V.; Cramer, C. J.; Truhlar, D. G. Universal Solvation Model Based on Solute Electron Density and on a Continuum Model of the Solvent Defined by the

Bulk Dielectric Constant and Atomic Surface Tensions. *The Journal of Physical Chemistry B* **2009**, *113* (18), 6378-6396.

(13) Perdew, J. P.; Ernzerhof, M.; Burke, K. Rationale for mixing exact exchange with density functional approximations. *The Journal of Chemical Physics* **1996**, *105* (22), 9982-9985.